



University
of Glasgow

Logakannan, K. P., Ruan, D., Rengaswamy, J., Kumar, S. and Ramachandran, V. (2023) Fracture locus of additively manufactured AlSi10Mg alloy. *Thin-Walled Structures*, 184, 110460. (doi: [10.1016/j.tws.2022.110460](https://doi.org/10.1016/j.tws.2022.110460))

Copyright © 2022 Elsevier Ltd. This is the author version of the work reproduced here under a Creative Commons Attribution-NonCommercial-NoDerivs 4.0 licence: <https://creativecommons.org/licenses/by-nc-nd/4.0/> .

There may be differences between this version and the published version. You are advised to consult the publisher's version if you wish to cite from it: <https://doi.org/10.1016/j.tws.2022.110460>

<https://eprints.gla.ac.uk/287996/>

Deposited on: 16 December 2022

Enlighten – Research publications by members of the University of Glasgow
<http://eprints.gla.ac.uk>

Fracture locus of additively manufactured AlSi10Mg alloy

Krishna Prasath Logakannan^{1,2}, Dong Ruan^{1,*}, Jayaganthan Rengaswamy³, S. Kumar⁴, and
Velmurugan Ramachandran^{2,*}

¹ School of Engineering, Swinburne University of Technology, Hawthorn, VIC 3122,
Australia

² Department of Aerospace Engineering, Indian Institute of Technology Madras, Chennai
600036, India

³ Department of Engineering Design, Indian Institute of Technology Madras, Chennai
600036, India

⁴ James Watt School of Engineering, University of Glasgow, Glasgow G12 8LT, UK

*Corresponding authors. Emails: druan@swin.edu.au and ramanv@iitm.ac.in

Abstract

In cellular structures, fracture occurs at various locations due to localized complex stress- and/or strain-state. Using the failure strain obtained from a conventional tensile test, the localized failure in cellular materials cannot be adequately predicted through finite element analysis owing to localized triaxial stress-state. Moreover, complex build orientation of different ligaments influences the macroscopic performance of cellular structures considerably. In order to accurately predict the failure of cellular structures using numerical approach, failure strain with respect to both the stress triaxiality and the build orientation ought to be considered. The fracture loci of Laser Powder Bed Fusion (LPBF) fabricated AlSi10Mg alloy were determined experimentally for different build orientations to develop a predictive capability. Moreover, quasi-static compression tests were performed on an additively manufactured re-entrant cellular structures and the experimental results were corroborated by the numerical predictions obtained using fracture loci. The numerical model which considers triaxial fracture

1 locus predicts the deformation mode and the fracture location of the re-entrant structure more
2 accurately than the model that considers a simple uniaxial tensile failure.
3
4
5
6

7 **Keywords:** Fracture locus; build orientation; cellular structure; Laser Powder Bed Fusion
8 additive manufacturing; AlSi10Mg alloy
9
10
11
12
13

14 **1. Introduction**

16 Deformation behavior and deformation related properties of the cellular structures are
17 dependent on both topology of structures and the parent materials from which structures are
18 made. For example, Poisson's ratio of cellular structures is geometry-dependent [1–4], while
19 the elastic modulus of a cellular structure is generally higher if the parent material is stiffer [5].
20 Materials with negative Poisson's ratio are gaining more attention because of their interesting
21 mechanical properties and application [6–10]. Re-entrant structure is a periodic cellular
22 structure which is well-known for its negative Poisson's ratio capabilities. Properties of re-
23 entrant structure can be controlled by varying its geometrical parameters [11]. Finite element
24 analysis (FEA) is an efficient tool to conduct geometrical parametric study and visualize the
25 stress or strain profiles at various sections and instants [12–14] at relatively low cost compared
26 with experimental tests. Therefore, FEA has been widely employed to simulate many
27 engineering structures including cellular structures. One of the influential parameters in FE
28 models for predicting deformation of cellular structures is failure strain of the parent material.
29 The failure strain and location of failure in a cellular structure are determined by localized
30 stress-state in the cellular structure and ductility of the parent material. To predict such failures
31 through FEA, failure criterion used should account for the localized stress-state and material
32 ductility.
33
34
35
36
37
38
39
40
41
42
43
44
45
46
47
48
49
50
51
52
53
54
55
56
57
58
59
60
61
62
63
64
65

There are several failure criteria available for conventional ductile metals. Bai et al. [15] reviewed different failure theories based on physics and empirical models. Physics based models [16,17] were developed via the theories of void nucleation and growth. Empirical models include but not limited to Johnson-Cook damage model [18], Bao-Wierzbicki model [19] and Bai-Wierzbicki model [20]. Most of the empirical models relate failure strain to stress triaxiality (η) and Lode angle parameter ($\bar{\theta}$). Stress triaxiality is a measurement of the relative degree of hydrostatic stress in a given stress-state and is calculated as the mean stress (σ_m) divided by the equivalent stress ($\bar{\sigma}$). Lode angle parameter relates the third deviatoric stress invariant to equivalent stress.

$$\eta = \frac{\sigma_m}{\bar{\sigma}} \quad (1)$$

$$\bar{\theta} = 1 - \frac{2}{\pi} \arccos \xi \quad (2)$$

$$\xi = \frac{27 J_3}{2 \bar{\sigma}^3} \quad (3)$$

where $\sigma_m = \frac{\sigma_1 + \sigma_2 + \sigma_3}{3}$, σ_1 , σ_2 and σ_3 are the principal stresses, ξ is the normalized third deviatoric stress invariant, and J_3 is the third deviatoric stress invariant. η and $\bar{\theta}$ are crucial for predicting failure strain under complex stress-state. Advanced fracture model such as DF 2014 [21] and Hosford-coulomb [22] provide better predictive capabilities by considering η and $\bar{\theta}$ in failure. Fracture locus (2D or 3D) of any material can be constructed by performing tests for various η and $\bar{\theta}$. For example, compression test yields negative triaxiality values because of negative mean stress and the value of negative triaxiality can be varied by changing the diameter to height ratio of the compression samples. Tensile tests yield positive triaxiality values. Fracture loci have been widely discussed in literature for conventional ductile metals [19,20,23–28].

Though there are several works on conventional metals, fracture locus for additive manufactured materials is still rare. Recently, fracture loci for additively manufactured 18-

1 Ni300 steel [29] and aluminium A357 [30] were developed. Roth et al.[31] performed
2 mechanical and metallographic characterization of AlSi10Mg manufactured through SLM
3 process. They constructed a 2D fracture locus for SLM printed and cast AlSi10Mg alloy. The
4 fracture locus was constructed using shear and tensile coupons and the curve for negative stress
5 triaxiality regime was extrapolated. However, they did not report the influence of build
6 orientation on fracture locus. Most additively manufactured (AM) materials normally exhibit
7 properties which tend to vary with respect to build orientation [32,33]. Dong et al. [32] reported
8 variations in Young's modulus, yield strength, elongation, and ultimate tensile strength of
9 coupons built in different orientations. The samples built along the vertical orientation
10 (perpendicular to the build platform) exhibited the least porosity and thus resulted in 13.5%
11 increase in yield strength and 29.5% increase in ultimate tensile strength compared to those of
12 coupons built at 35.5° with respect to powder bed. Maconachie et al. [33] reported a noticeable
13 difference in mechanical properties for samples built along different orientations under both
14 quasi-static and dynamic loading conditions. Other studies [34–37] also reported orientation-
15 dependent mechanical properties.

16
17
18
19
20
21
22
23
24
25
26
27
28
29
30
31
32
33
34
35
36
37
38
39
40
41
42
43
44
45
46
47
48
49
50
51
52
53
54
55
56
57
58
59
60
61
62
63
64
65
Periodic structures possess walls/struts which are built along different orientations and
their properties could vary based on orientation [38]. They have several nodes/junctions where
two or more walls/struts meet, and stresses become localized at these locations under loading.
Therefore, there is a need for sophisticated testing of parent material to predict failure of the
cellular structures. Moreover, the influence of failure criteria on the prediction of deformation
behavior of cellular materials using FE models is not extensively discussed in the literature.
Fracture loci with respect to different stress triaxiality values are essential to accurately predict
the failure of cellular materials. However, to the best knowledge of the authors, fracture loci of
the additively manufactured AlSi10Mg alloy for different print orientations and its significance
in predicting failure of cellular structures is not reported. Also, the discrepancy in geometry at

critical locations is also crucial, because it could lead to early failure, especially in 3D lattice structures [39].

In this work, the fracture loci of additively manufactured AlSi10Mg alloy were determined and the effect of build orientations was explored. Samples were fabricated via Laser Powder Bed Fusion (LPBF) using AlSi10Mg alloy powder feedstock. Uniaxial compressive, shear, and tensile tests were performed to obtain failure strains for different stress triaxiality values. Numerical simulations were performed to measure the triaxiality values in the compressive, shear, and tensile tests. Fracture loci of additively manufactured AlSi10Mg alloy were obtained for different orientations and employed in the simulation of additively manufactured re-entrant structures to demonstrate the significance of fracture locus in predicting their deformation characteristics and load carrying capacity.

2. Material and Mechanical tests

2.1. Material and additive manufacturing

Test coupons were fabricated through LPBF process using AlSi10Mg powder feedstock and the chemical composition of the feedstock is given in Table 1. The average size of powder particles was 32 μm . Plates (150 mm \times 50 mm \times 4 mm) and rods (15 mm diameter and 180 mm height) were printed along three different orientations, namely, horizontal, inclined, and vertical. Figure 1 describes the plate/rod orientations with respect to the powder bed. Printed plates and rods were subsequently machined to obtain test coupons with required shapes and dimensions to perform uniaxial compression, shear, and uniaxial tensile tests as per international standards. The sizes of printed plates, rods, and re-entrant structure were determined based on the printing constraints (e.g., the build volume of the 3D printer) and load cell capacity of the test machines.

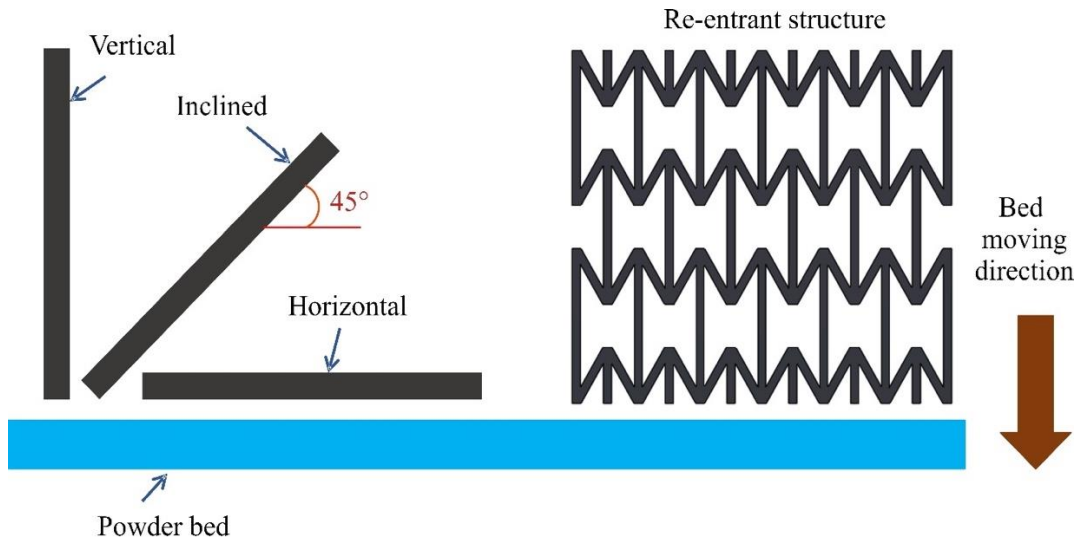


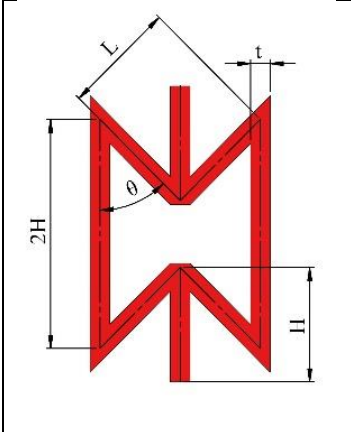
Figure 1. Sketch showing the build orientation of plates, rods, and re-entrant samples with respect to print bed.

Table 1. Chemical composition of printed aluminum alloy AlSi10Mg (data provided by the supplier: ECKART TLS GmbH)

| Elements | Al | Si | Mg | Fe | Cu | Zn | Ti | Mn | Ni | Pb | Sn |
|-----------------|---------|------|------|------|-------|-------|-------|-------|-------|-------|---------|
| Composition (%) | Balance | 9.76 | 0.41 | 0.16 | 0.001 | 0.001 | 0.004 | 0.003 | 0.003 | 0.001 | <0.0005 |

Two samples of re-entrant cellular structure were printed such that vertical walls were aligned to the vertical build orientation. Geometrical parameters of the printed re-entrant structure are given in Table 2. Printed samples were sandblasted to remove the residual powders. The process parameters were kept the same for all the test coupons and re-entrant structures. The average density of the printed rods and plates were 2.62 g/cm^3 , 2.62 g/cm^3 , and 2.60 g/cm^3 for horizontal, inclined, and vertical directions, respectively.

Table 2. Dimensions of a unit cell of re-entrant structure

| | | | | |
|---|--------|--------|--------------|--------|
|  | L (mm) | H (mm) | θ (°) | t (mm) |
| | 12 | 12 | 30 | 2 |

2.2. Micro-Computed Tomography characterization

One printed re-entrant structure sample was scanned through Micro-Computed Tomography (Micro-CT) and a 3D image is shown in Fig. 2. Scanned image reveals that the printed re-entrant structure exhibits few surface pores on the vertical struts. One of the scanned 2D images was used as a reference to plot the sketch of re-entrant structure in SOLIDWORKS. Drawn sketch was extruded to model the re-entrant structure which was used in the subsequent finite element analysis.

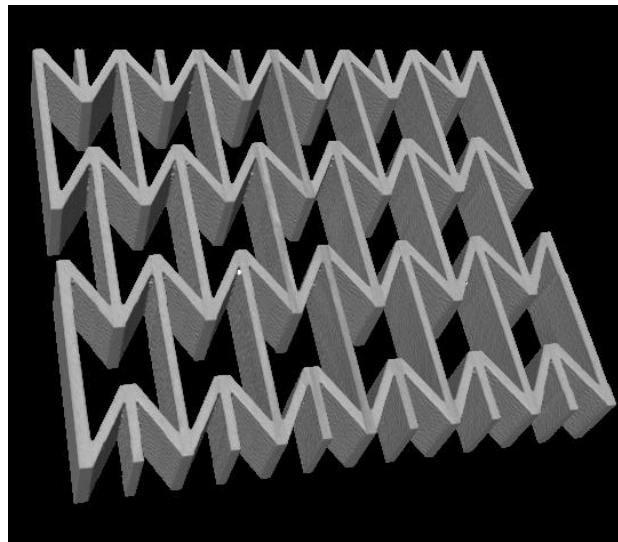


Figure 2. 3D image of a printed re-entrant structure obtained using Micro-Computed Tomography. Dimensions of the shown re-entrant structure are 89.23 mm \times 82.33 mm \times 15 mm.

2.3. Heat treatment

Coupons in as-printed condition tend to be harder, stronger (higher yield and ultimate strengths), while less ductile [40,41]. Heat treatment was conducted on as-printed coupons to improve their ductility by relieving internal stresses and increasing grain size. To understand the effect of heat treatment on the printed coupons, hardness and tensile tests were conducted on the heat-treated coupons. Heat treatments were carried out in a muffled furnace with an accuracy of $\pm 5^\circ \text{C}$. Coupons were cut from a plate printed along the horizontal direction and heat treated by two different processes, stress relieving (SR) and solution treatment (ST), respectively. SR was performed at 300°C for 2 hours followed by air cooling. ST was carried out at 500°C for 1 hour and then water quenched. Temperatures for the heat treatment were chosen based on the results of previous studies [40,41].

2.4. Mechanical tests

2.4.1 Mechanical tests to obtain the material properties

Hardness test was conducted on all heat-treated coupons, as it gives preliminary indication about the strength of the material. Vickers hardness test was conducted on $10 \text{ mm} \times 10 \text{ mm} \times 4 \text{ mm}$ test coupons under 1 kg load with a dwell time of 10 seconds. Coupons were cut from fabricated plates built in the horizontal orientation. At least three measurements were made for each coupon.

A 2D fracture locus is constructed by plotting stress triaxiality factor in abscissa and failure strain in the ordinate. To construct it, a range of coupon tests exhibiting at least five different stress triaxiality values were conducted. As mentioned in the Introduction section, uniaxial compression, shear, and tensile tests exhibit negative, zero, and positive stress triaxialities, respectively. In uniaxial compression, stress triaxiality value is affected by the ratio of diameter-to-height of the cylindrical coupons. Therefore, two types of coupons with

1 different diameter-to-height ratios were tested. For tensile tests, presence of notch creates
 2 higher stress triaxiality values than standard tensile test coupons and the magnitude of
 3 triaxiality is influenced by the notch dimensions. As such, apart from the standard tensile test,
 4 triaxiality is influenced by the notch dimensions. As such, apart from the standard tensile test,
 5 two additional tensile test coupons with two different notch radii were also tested to obtain
 6 additional triaxiality data points for the fracture locus. In this work, failure strains obtained
 7 from these six types of coupon tests (two compression, one shear and three tension) were used
 8 to construct the fracture locus. Uniaxial compression tests on solid cylindrical coupons were
 9 carried out according to ASTM E9 standard. Cylinder diameter was kept as 8 mm and height
 10 was varied to maintain diameter to height (D/H) ratio of 1 and 0.67, respectively. Figure 3(a)
 11 shows the sketch of a compression test coupon (D/H = 0.67). Compression tests were carried
 12 out on Zwick Roell universal testing machine (UTM) of 100 kN load-cell capacity. The bottom
 13 platen was fixed, and the top platen was moved downwards at a speed of 10 mm/min. Grease
 14 was applied between the test coupons and the platens to reduce friction.
 15
 16
 17
 18
 19
 20
 21
 22
 23
 24
 25
 26
 27
 28
 29
 30
 31
 32
 33
 34
 35
 36
 37
 38
 39
 40
 41
 42
 43
 44
 45
 46
 47
 48
 49
 50
 51
 52
 53
 54
 55
 56
 57
 58
 59
 60
 61
 62
 63
 64
 65

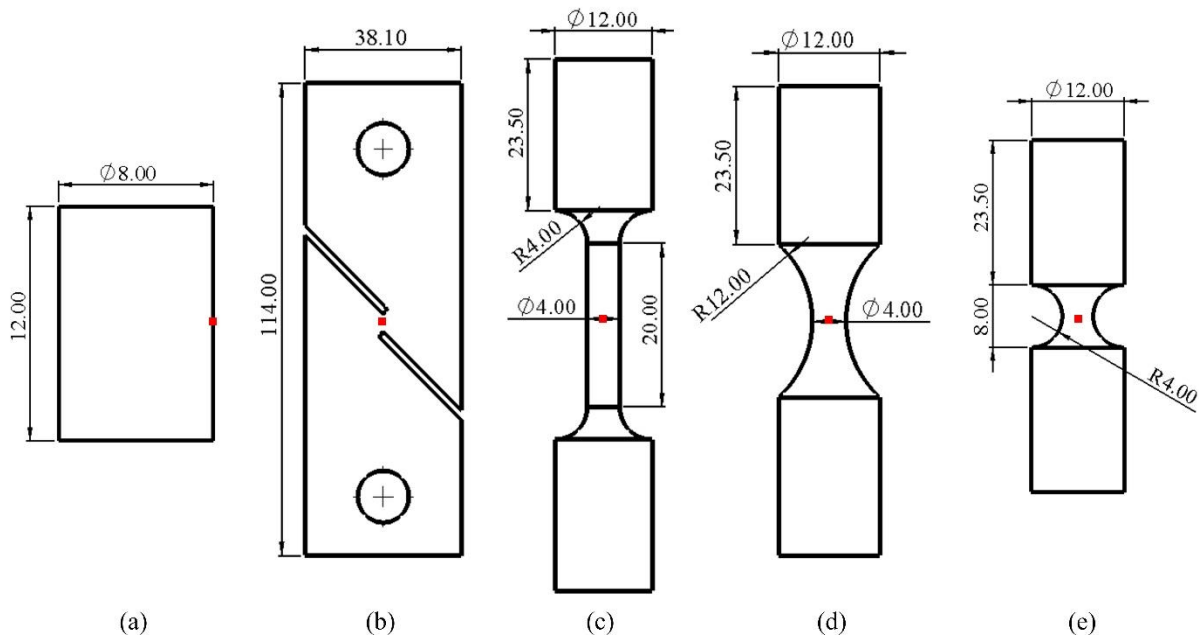


Figure 3. Dimensions of coupons and the positions used to calculate the triaxiality factors: (a) uniaxial compression (D/H=0.67); (b) shear; (c) uniaxial tensile (non-notched); (d) tensile (large notch); (e) uniaxial tensile (small notch). Note: all dimensions are in mm, and they are not to scale.

1 Shear test coupons (Fig. 3b) were cut from printed plates, according to ASTM B831.
2 Thickness of the shear test coupons were 4 mm. Tests were performed on an Instron machine
3 with a 5 kN load-cell capacity at the speed of 2 mm/min. Speckle pattern for digital image
4 correlation (DIC) was made on the shear zone and images were captured during the test at a
5 rate of 5 frames/second.
6
7
8
9
10

11 Non-notch tensile test coupons (Fig. 3c) were machined from the printed rods and
12 dimensions of the coupons were chosen according to ASTM E8. Uniaxial tensile tests were
13 carried out at the speed of 2 mm/min. Gauge diameter was fixed at 4 mm for all tensile coupons.
14 Apart from the above, tensile coupons with two different notch diameters were also machined
15 to achieve higher triaxiality values. For notched tensile coupons, the minimum diameter of the
16 gauge section was maintained at 4 mm and notch radii were 12 mm and 4 mm for large notch
17 (Fig. 3d) and smaller notch (Fig. 3e) coupons, respectively. Speckle patterns for DIC were
18 made on the gauge section for all tensile coupons and images were captured during the test at
19 the rate of 5 frames/second. Captured DIC images from all the shear and uniaxial tensile tests
20 were analyzed using VIC-2D software supplied by Correlated Solutions. The subset and step
21 sizes used for the DIC image processing were 15 and 3, respectively. Fracture strain was
22 calculated using DIC as follows. For the shear tests, the average shear strain over the shear
23 zone at the time of fracture was considered as the shear failure strain. For the tensile tests, the
24 average axial strain reduced cross-section at the time of fracture was considered as the tensile
25 failure strain. Failure strains for the compression tests were determined by monitoring the onset
26 of crack initiation on the external surface [24]. The pixel/mm ratio for shear tests and tensile
27 tests are 20 and 28, respectively. For all the mechanical tests, at least three coupons were tested
28 for each test condition. Summary of material tests is provided in Table 3.
29
30
31
32
33
34
35
36
37
38
39
40
41
42
43
44
45
46
47
48
49
50
51
52
53
54
55
56
57
58
59
60
61
62
63
64
65

Table 3. Summary of the mechanical tests to obtain the material properties

| Test type | Coupon type |
|----------------------|--|
| Uniaxial compression | Solid cylinder (diameter/height =1), machined from printed rods |
| | Solid cylinder (diameter/height =0.67) (Fig. 3a), machined from printed rods |
| Shear | Pin ended sheet (Fig. 3b), cut from printed plates |
| Uniaxial tensile | Non-notch (Fig. 3c), machined from printed rods |
| | Notch with radius of 12 mm (Fig. 3d), machined from printed rods |
| | Notch with radius of 4 mm (Fig. 3e), machined from printed rods |

2.4.2 Quasi-static compression test: Cellular re-entrant structures

Re-entrant samples were subjected to quasi-static compression on Zwick Roell universal testing machine (UTM) of 100 kN capacity at a speed of 10 mm/min. The deformed shapes of the re-entrant structure were captured using a monochrome camera at the rate of 5 frames/second. The nominal stress-strain curve was recorded through the software available with the machine setup. The nominal stress and strain of the structure are defined and calculated as the ratios of force over the original cross-sectional area, and displacement over the original height of the structure, respectively.

3. Numerical simulation

Numerical simulations were carried out using commercial finite element (FE) package ABAQUS/Explicit. Four different models were developed to simulate uniaxial compression of solid cylindrical coupon, shear tests, uniaxial tensile tests (non-notched and notched), and uniaxial compression of a re-entrant structure. Isotropic elastic-plastic material model was employed for all the cases. Elastic modulus and the Poisson's ratio of AlSi10Mg were taken as 70 GPa and 0.33 respectively. Plastic material properties were fed to the model by taking multiple points from the coupon tests. The true stress-strain curve of the compression coupon with $D/H = 0.67$ (shown in Fig. 3a) was used in the FE model for compression of solid

1 cylinders. The true stress-strain curve of tensile coupons shown in Fig. 3(c) was used in the FE
2 models for shear and tensile coupons, as well as the FE model of the re-entrant structure. Mesh
3 sizes used in all the models were determined based on mesh convergence studies. Since we
4 considered rate-independent plasticity in all these cases, loading speeds in the FE models were
5 higher than those of experimental tests to reduce the computational time. However, it was
6 ensured that the chosen velocity did not introduce a significant dynamic effect (i.e., the kinetic
7 energy is less than 0.14% of the total energy for all the FE models).
8
9

10
11
12
13
14
15
16 For the compression model of the coupon with $D/H = 0.67$ shown in Fig. 3(a), the solid
17 cylinder was modelled and meshed using C3D8R elements of 0.5 mm size. Modelled cylinder
18 was compressed between two rigid platens. Bottom platen was fixed, and top platen was moved
19 downward at the speed of 50 mm/s to compress the cylinder. Surface to surface interaction was
20 set between the cylinder end faces and the corresponding platen, and friction coefficient was
21 set as 0.1. The purpose of simulating the compression test is to calculate the stress triaxiality
22 value, and thus it is crucial to mimic the experimental stress-strain curve. Therefore, the friction
23 coefficient was adjusted for the best match with experimental test results. Shear coupon shown
24 in Fig. 3(b) was modelled and meshed using shell element (S4R), as the out of plane thickness
25 is just 4 mm. Finer mesh of size 0.25 mm was used near shear zone and coarse mesh of size of
26 3 mm was used over the remaining area.
27
28
29
30
31
32
33
34
35
36
37
38
39
40
41
42

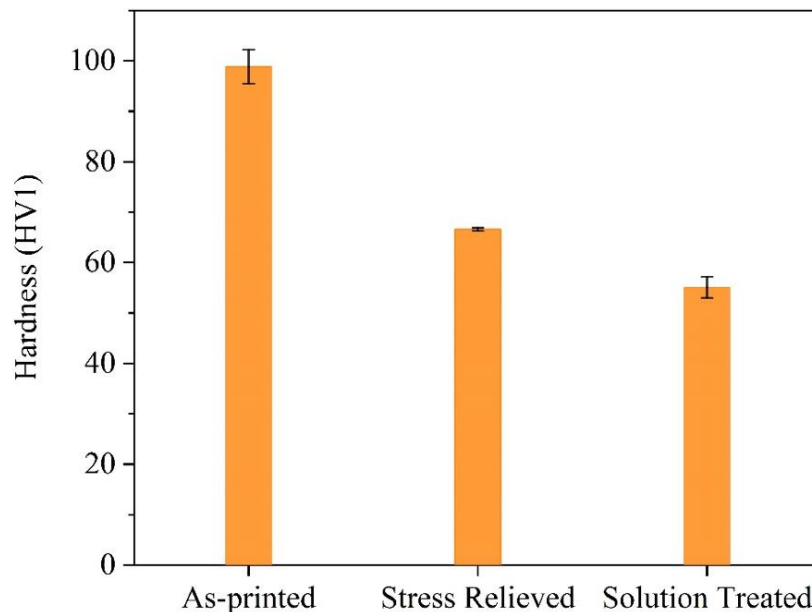
43 Axisymmetric elements of 0.25 mm size were used to model the gauge sections of all the
44 tensile coupons shown in Figs. 3(c), (d), and (e). The bottom end of each gauge section was
45 fixed, and the top end of each gauge section was given an axial velocity of 20 mm/s to apply
46 tensile loading. The FE model for the compression of the re-entrant structure followed a similar
47 setup of compression model of cylindrical compression coupons, except that the compression
48 speed was maintained at 150 mm/s. Also, a general contact was used for all the surface of the
49 re-entrant structure. Surface to surface contacts were employed between the re-entrant structure
50
51
52
53
54
55
56
57
58
59
60
61
62
63
64
65

1 end face and the corresponding platen. Static friction coefficient of 0.1 was used for both types
2 of contacts. Due to the challenges in experimentally measuring the stress triaxiality, the stress-
3 state of each simulated coupon at a specific location is numerically examined to determine the
4 stress triaxiality. It is to be noted that the simulations were carried out only till the fracture
5 strain obtained from the experiments. The fracture strain values used further in this work were
6 experimentally determined values.
7
8
9
10
11
12
13
14
15
16

17 4. Results and discussion

18 4.1. Effect of heat treatment

19 Figure 4 shows the Vickers hardness measured from as-printed and heat treated 10 mm × 10
20 mm × 4 mm test coupons. The average hardness values exhibited by as-printed, SR, and ST
21 coupons are 98.84 VH1, 65.56 VH1, and 55 VH1, respectively. This indicates that the heat
22 treatment has significantly reduced the hardness of the printed material. ST coupons are the
23 softest compared to the other two conditions.
24
25
26
27
28
29
30
31
32
33



34
35
36
37
38
39
40
41
42
43
44
45
46
47
48
49
50
51
52
53
54
55
56
57
58
59
60
61
62
63
64
65
Figure 4. Vickers hardness of as-printed and heat treated 10 mm × 10 mm × 4 mm test coupons.

Tensile coupon cut from a printed plate along the horizontal orientation for each heat-treated condition was tested and results are shown in Fig. 5. Yield strength and the ultimate strength of as-printed tensile coupons are 214 MPa and 307 MPa, respectively. After heat treatment, yield strength has reduced to 192 MPa and 184 MPa, for SR and ST tensile coupons, respectively. Ultimate strength follows a similar trend. The average failure strain of as-printed coupons is 0.1 and it has increased to 0.17 for SR and 0.2 for ST coupons. This implies that the ductility of the tensile coupons is improved upon heat treatment. The trend of strength and failure strain matches with the trend observed in the literature [40,41]. SR tensile coupons show a good combination of ductility and strength. Therefore, all the coupons and re-entrant structure samples were SR heat treated before tests.

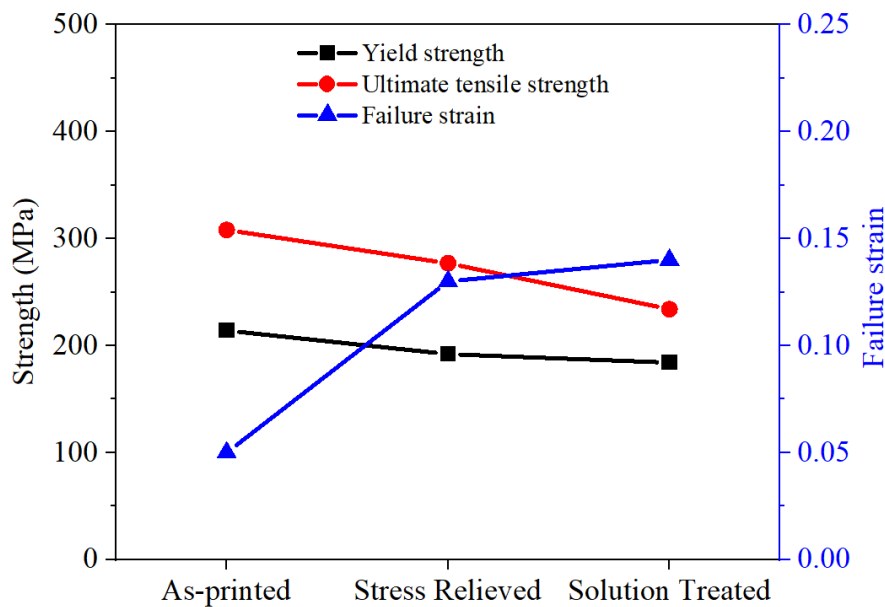


Figure 5. Yield strength, ultimate strength, and failure strain obtained from uniaxial tensile tests of printed coupons along the horizontal direction under various heat treatment conditions.

4.2. Mechanical test results of coupons

Uniaxial compression, shear, and uniaxial tensile tests were conducted on coupons fabricated along all three build orientations. Results of the tests are discussed in this section.

4.2.1. Uniaxial compression tests of coupons

Figures 6 and 7 show the stress-strain curves of coupons obtained from the uniaxial compression tests. The curves obtained were repeatable for all build orientations and D/H ratios except for D/H=1 printed at horizontal orientation. This could be due to variation in manufactured specimen. The stress increases linearly with strain till the compressive strain of 0.025 for almost all the coupons. In this paper, compressive strength is defined as the value of compressive stress at the compressive strain of 0.5. Compressive strengths obtained for different orientations and different D/H values are shown in Fig. 8. For D/H=1, the maximum average compressive strength is obtained for horizontal orientation with the value of 714 MPa \pm 30 MPa. Inclined and vertical orientations exhibit almost similar average compressive strength (approximately 660 MPa). Whereas for D/H= 0.67, coupons printed along the inclined orientation exhibit the lowest average compressive strength (593 MPa \pm 19.5 MPa) and vertical orientation shows the highest average compressive strength (615 MPa \pm 60 MPa). During compression, failure was not observed for coupons with D/H=1, however, it was observed for D/H=0.67. The average values of failure strain obtained for horizontal, inclined, and vertical orientations are 0.59 \pm 0.01, 0.69 \pm 0.01, and 0.73 \pm 0.01, respectively.

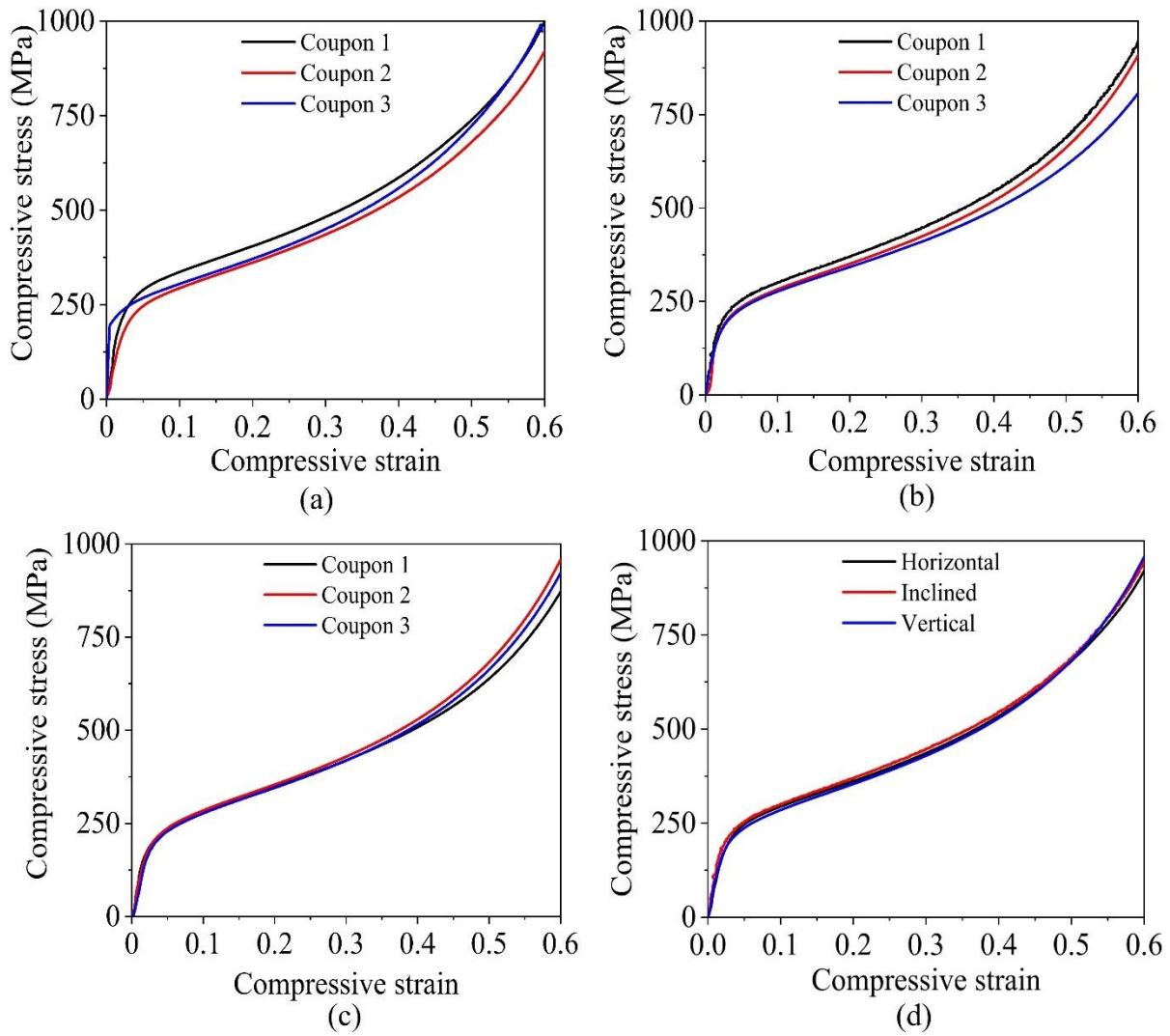


Figure 6. Stress-strain curves obtained from the uniaxial compression tests of solid cylindrical coupons of $D/H = 1$ printed along the: (a) horizontal; (b) inclined; (c) vertical; and (d) all orientations.

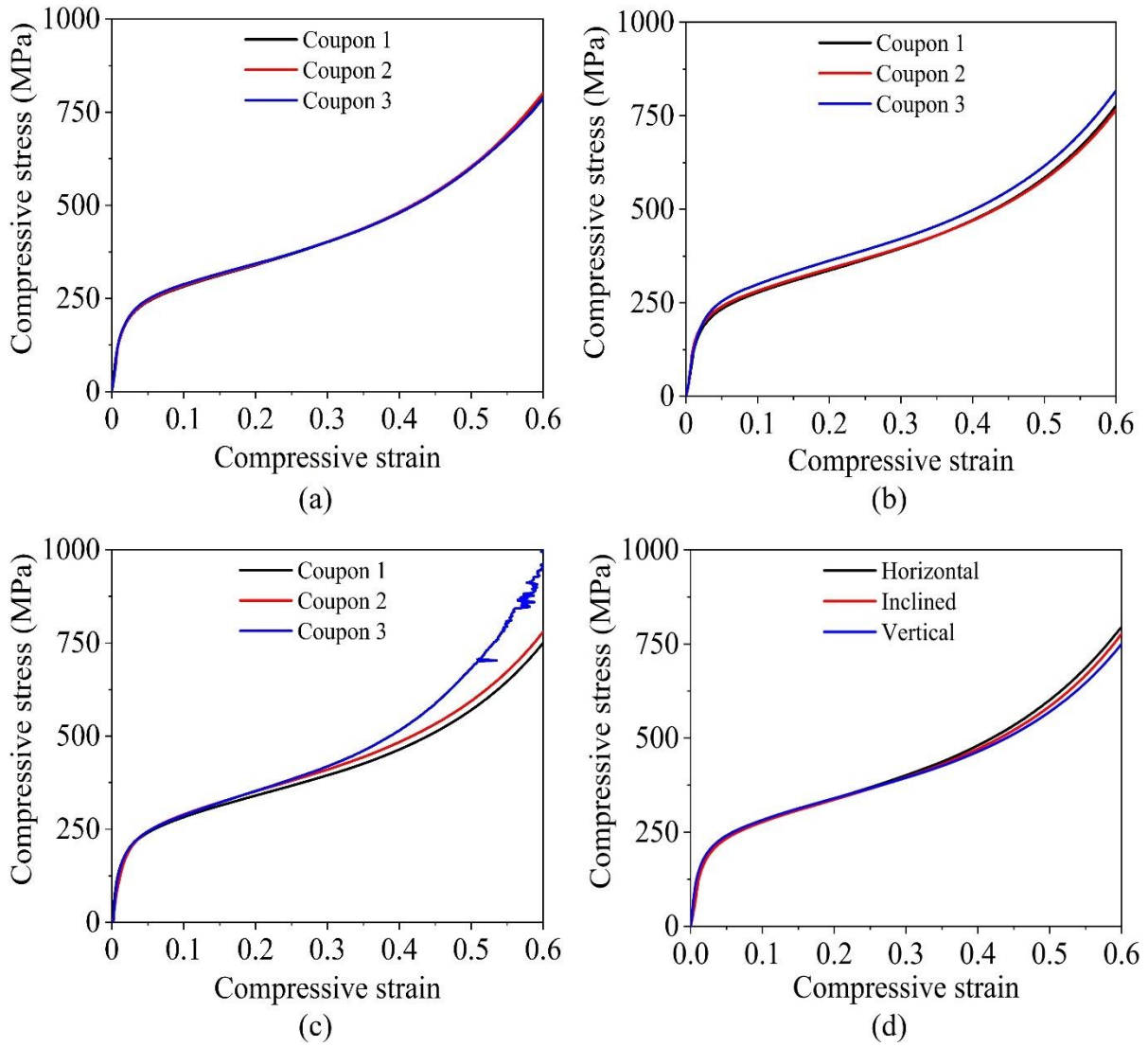


Figure 7. Stress-strain curves obtained from the uniaxial compression tests of solid cylindrical coupons of $D/H = 0.67$ printed along the: (a) horizontal; (b) inclined; (c) vertical; and (d) all orientations.

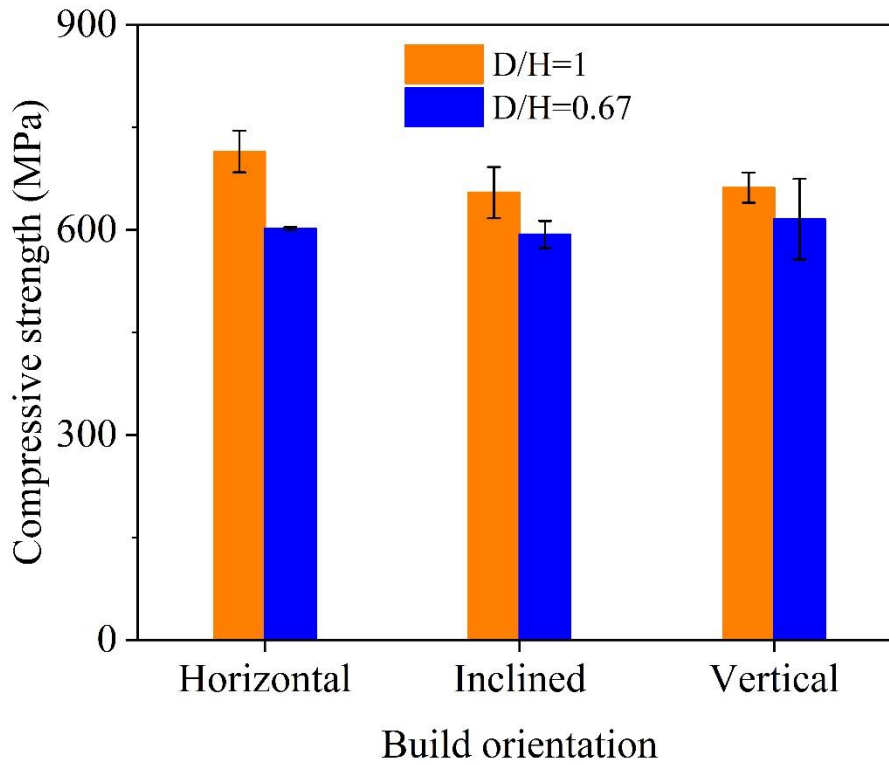


Figure 8. Compressive strength values obtained from the uniaxial compression tests of cylindrical coupons printed along the three orientations and with different D/H values.

4.2.2. Shear tests of coupons

Shear stress-strain curves obtained from the experimental tests are shown in Fig. 9. The shear failure strain values were obtained through DIC. Shear stress is defined as the force divided by the shear area. The average values of the maximum shear strength for horizontal, inclined, and vertical orientations are 167 ± 2.66 MPa, 158 ± 5.8 MPa, and 142 ± 4.3 MPa, respectively. The average failure strain values for horizontal, inclined, and vertical orientations are 0.27 ± 0.03 , 0.35 ± 0.07 , and 0.36 ± 0.03 , respectively. Coupons printed along the horizontal orientation show better shear strength and lower failure strain when compared with the coupons printed along the other two orientations. Three repeated tests were conducted on coupons printed along each orientation (Fig. 9). Variations are observed in the stress-strain curves due to the manufacturing defects. The coupons printed along the vertical orientation exhibited least variation in the stress-strain curve when compared with coupons built along the other two

orientations. At least two test results (i.e., Coupons 1 and 2 in Fig. 9a and b) agreed well for each of the horizontal and inclined orientations.

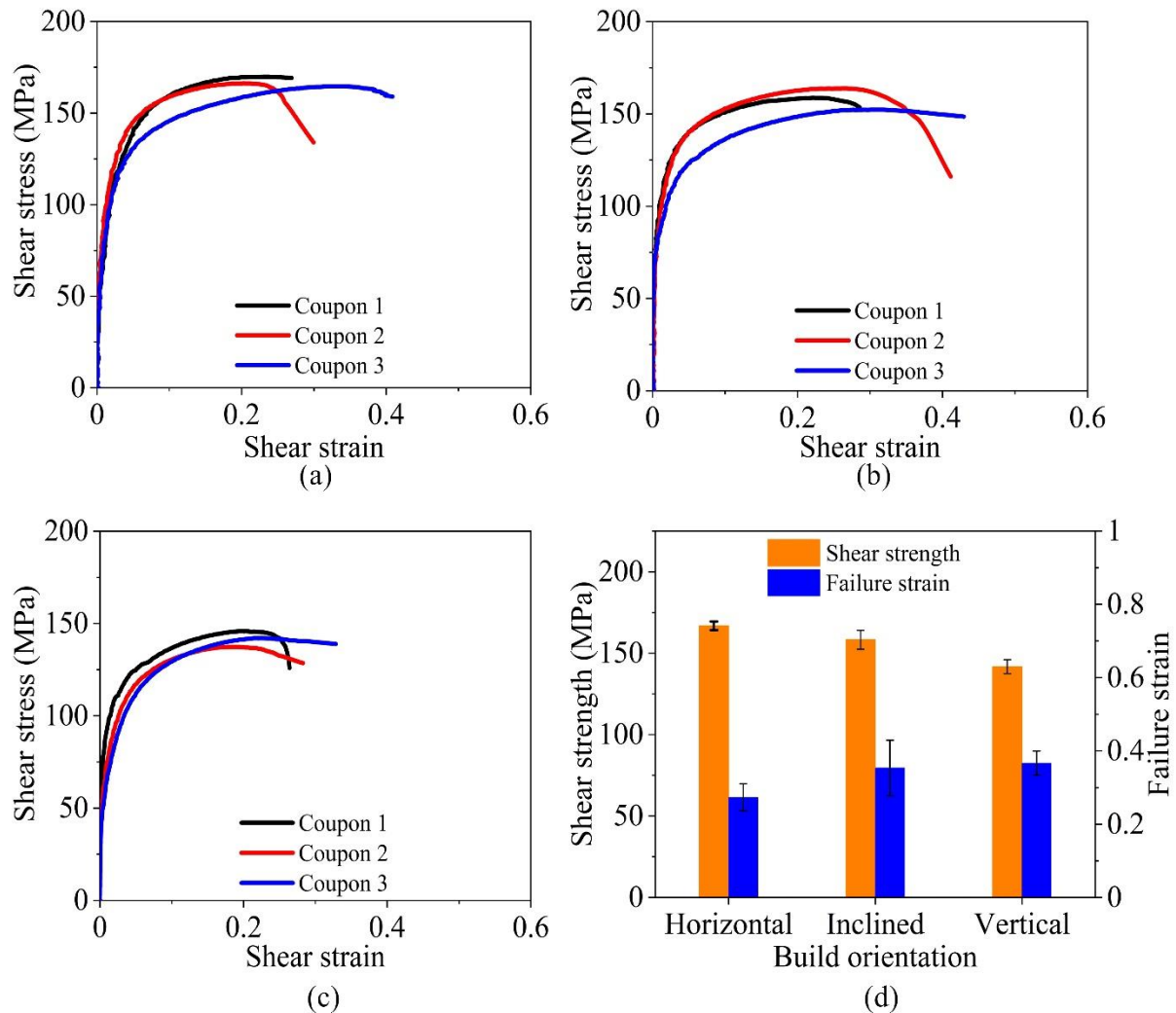


Figure 9. Shear test results of coupons printed along the three build orientations: (a) horizontal; (b) inclined; (c) vertical; and (d) shear strength and failure strain.

4.2.3. Uniaxial tensile tests of coupons

Figure 10 shows the stress-strain curves obtained from the uniaxial tensile tests of coupons without notch printed along the three build orientations. The average ultimate strengths observed for horizontal, inclined, and vertical orientations are 226 ± 3.67 MPa, 235 ± 5.24 MPa, and 222 ± 8.9 MPa, respectively, and the average failure strain values are 0.13 ± 0.01 , 0.15 ± 0.02 , and 0.11 ± 0.01 , respectively. Results show that coupons printed along the inclined

orientation possess the maximum strength and ductility, followed by those printed along the horizontal and vertical orientations. The variation of strength and failure strain with respect to different orientations is not significant. The yield strength of the coupons printed along the horizontal orientation show significant variations (Fig. 10a). However, the differences in the ultimate strength and failure strain, which are the two parameters of interests in this study, are small. Moreover, the coupons printed along the inclined orientation display different yield strengths and failure strains, the ultimate strengths are similar (Fig. 10b). Coupons printed along the vertical orientation exhibit the best repeatability in terms of yield strength, ultimate strength and failure strain (Fig. 10c).”

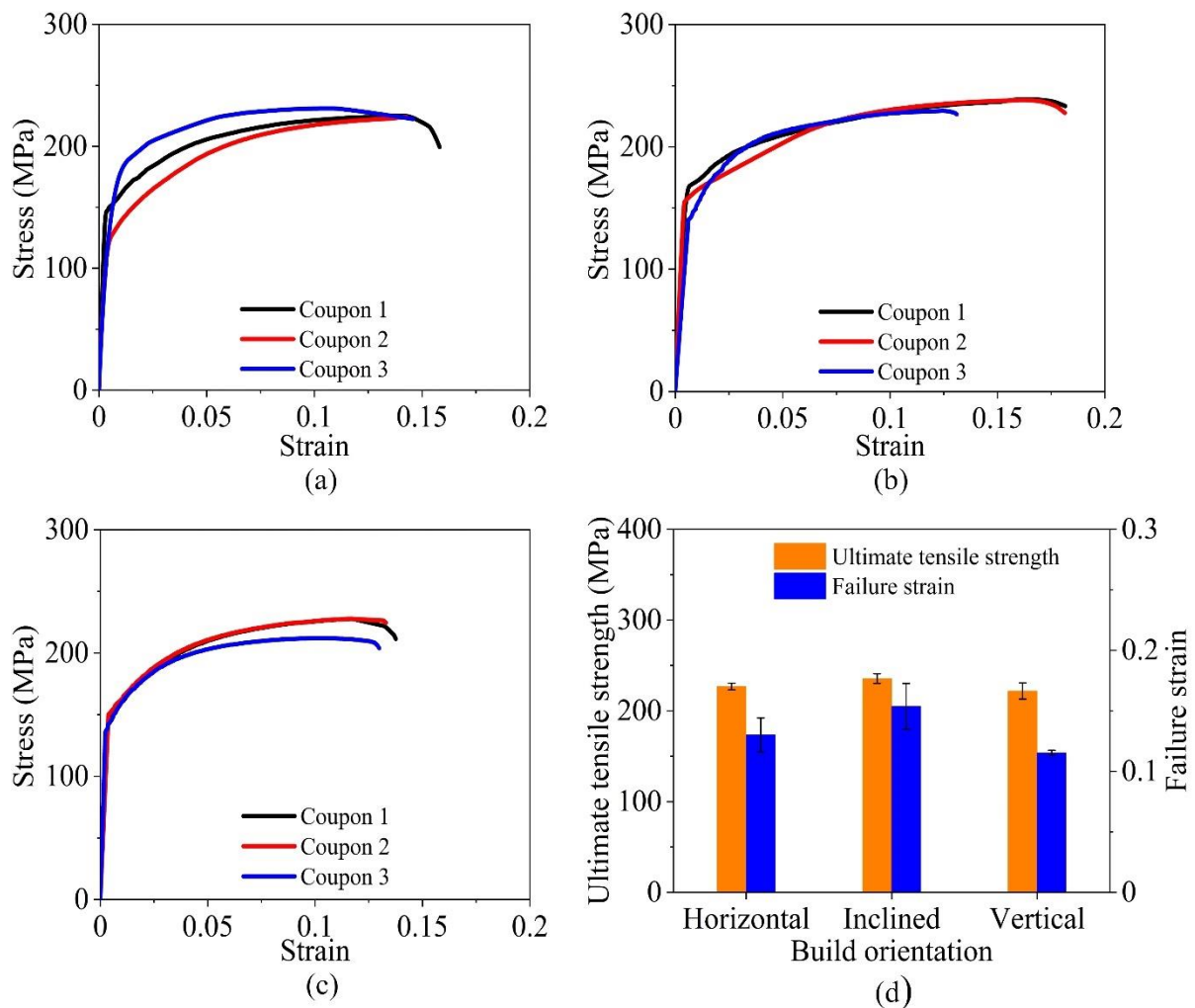


Figure 10. Uniaxial tensile test results of coupons without notch printed along the three build orientations: (a) horizontal; (b) inclined; (c) vertical; and (d) ultimate tensile strength and failure strain.

The stress-strain curves obtained from the tensile tests of notched coupons (R=12 and R=4) are shown in Figs. 11 and 12 respectively. Coupons printed along the inclined orientation displays the maximum strength for both the notched coupons and non-notched coupons. Irrespective of orientation, introduction of notch reduces the failure strain of the material significantly. The average failure strain of coupons with a small notch (R= 4 mm) is slightly higher than that of coupons with a large notch (R = 12 mm) for inclined and vertical orientations. However, for horizontal orientation, the average failure strain is reduced slightly from 0.045 (large notch) to 0.04 (small notch).

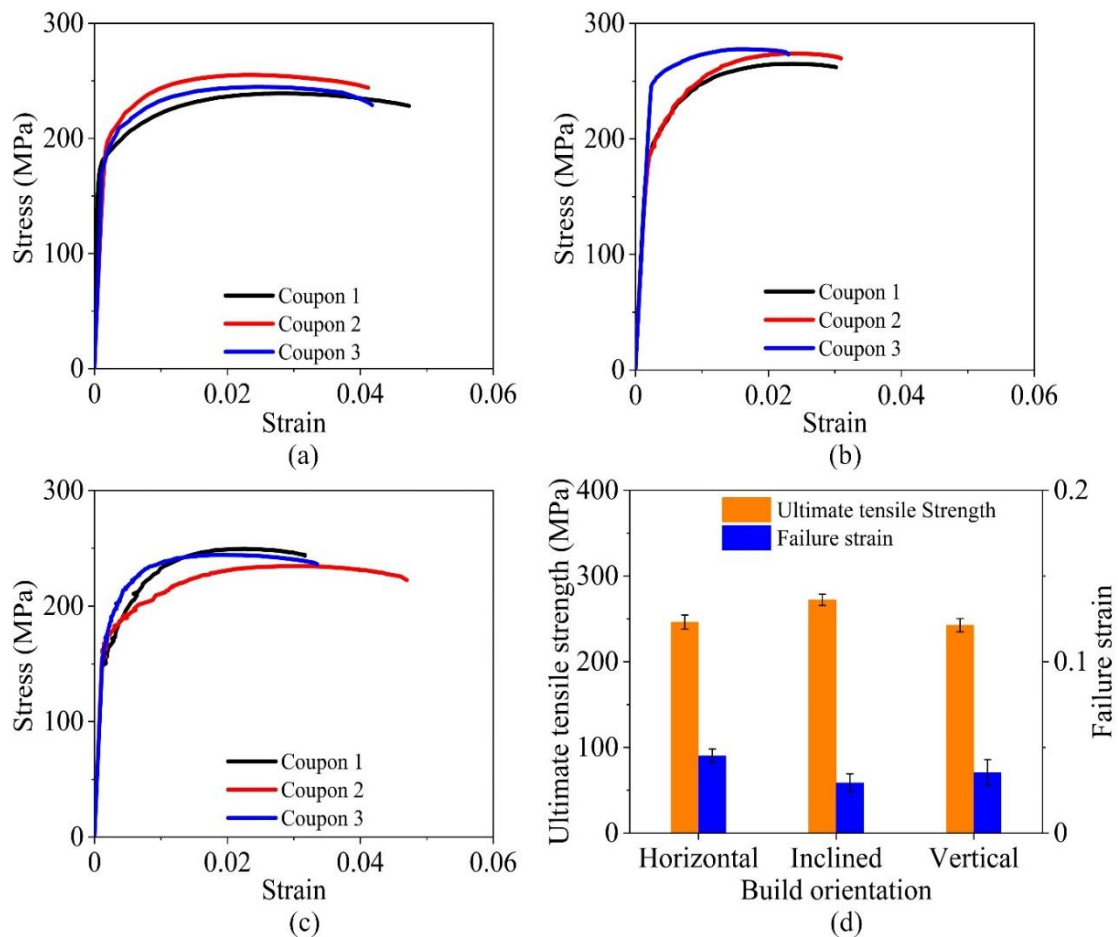


Figure 11. Tensile test results of notched coupons (R=12 mm) printed along the three build orientations: (a) horizontal; (b) inclined; (c) vertical; and (d) ultimate tensile strength and failure strain.

For notched tensile coupons with R=12 mm printed along the horizontal orientation, the yield strengths are similar, ultimate strength and fracture strain vary by 7% and 9%, respectively

(Fig. 11a). For the same type of coupons printed along the inclined and vertical orientations, at least two stress-strain curves are close to each other and have very similar yield strength, ultimate strength and fracture strain (Fig. 11b and c). For notched tensile coupons with R=4 mm, two stress-strain curves agree with each other for each print orientation (Fig. 12a, b and c). The largest variation is observed in the yield strength and failure strain for coupons printed along the inclined orientation.

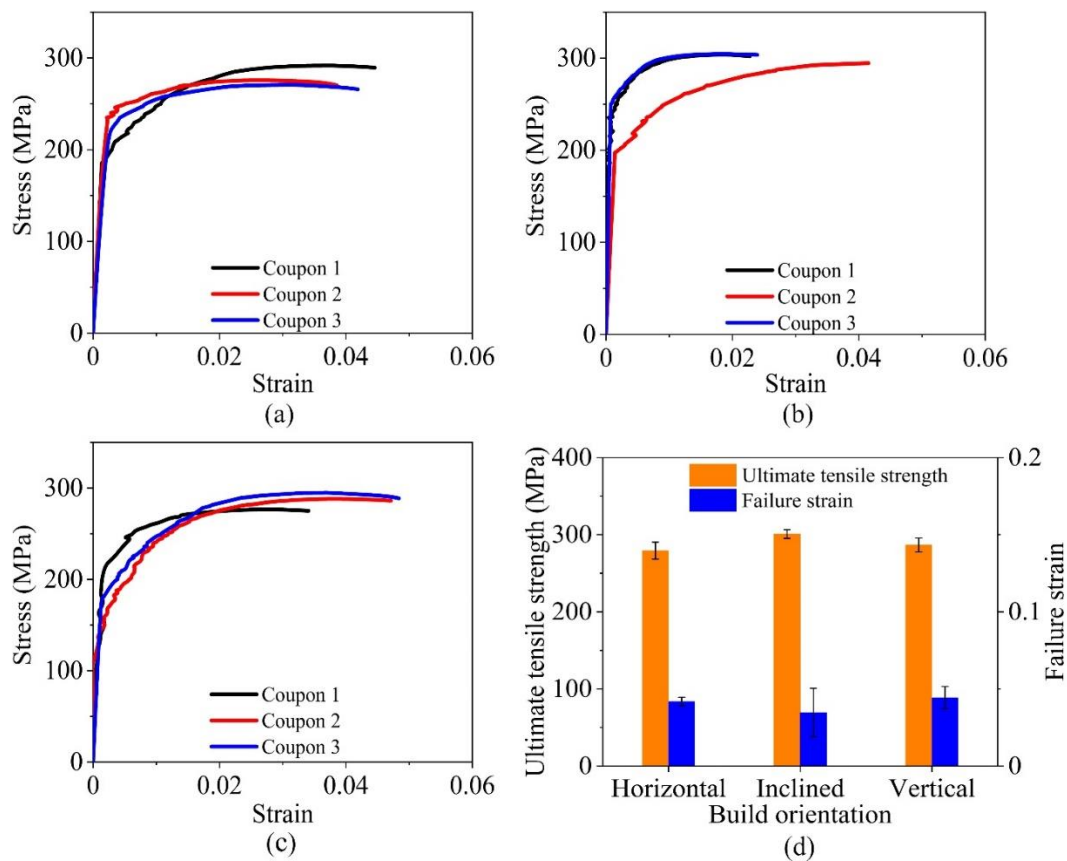


Figure 12. Tensile test results of notched coupons (R=4 mm) for various build orientations: (a) horizontal; (b) inclined; (c) vertical; and (d) ultimate tensile strength and failure strain.

4.3. Validation of FE models and determination of triaxiality values

Results of the numerical simulations of uniaxial compression, shear, and uniaxial tensile (non-notched and notched) tests were compared with the experimental results in Figure 13. Since at least two experimental results per test condition match well, only one representative experimental curve per test condition is shown in Fig. 13. Table 4 shows the coupon details

used for FE model validation. The numerically simulated and experimentally measured stress-strain curves match very well for all the loading conditions. This indicates that these FE models are precise and valid. The strain value obtained from the numerical simulation is similar to the experimental measurement where strain values were averaged over the gauge region for shear and tensile coupons. Compressive strain was obtained using displacement of the platen.

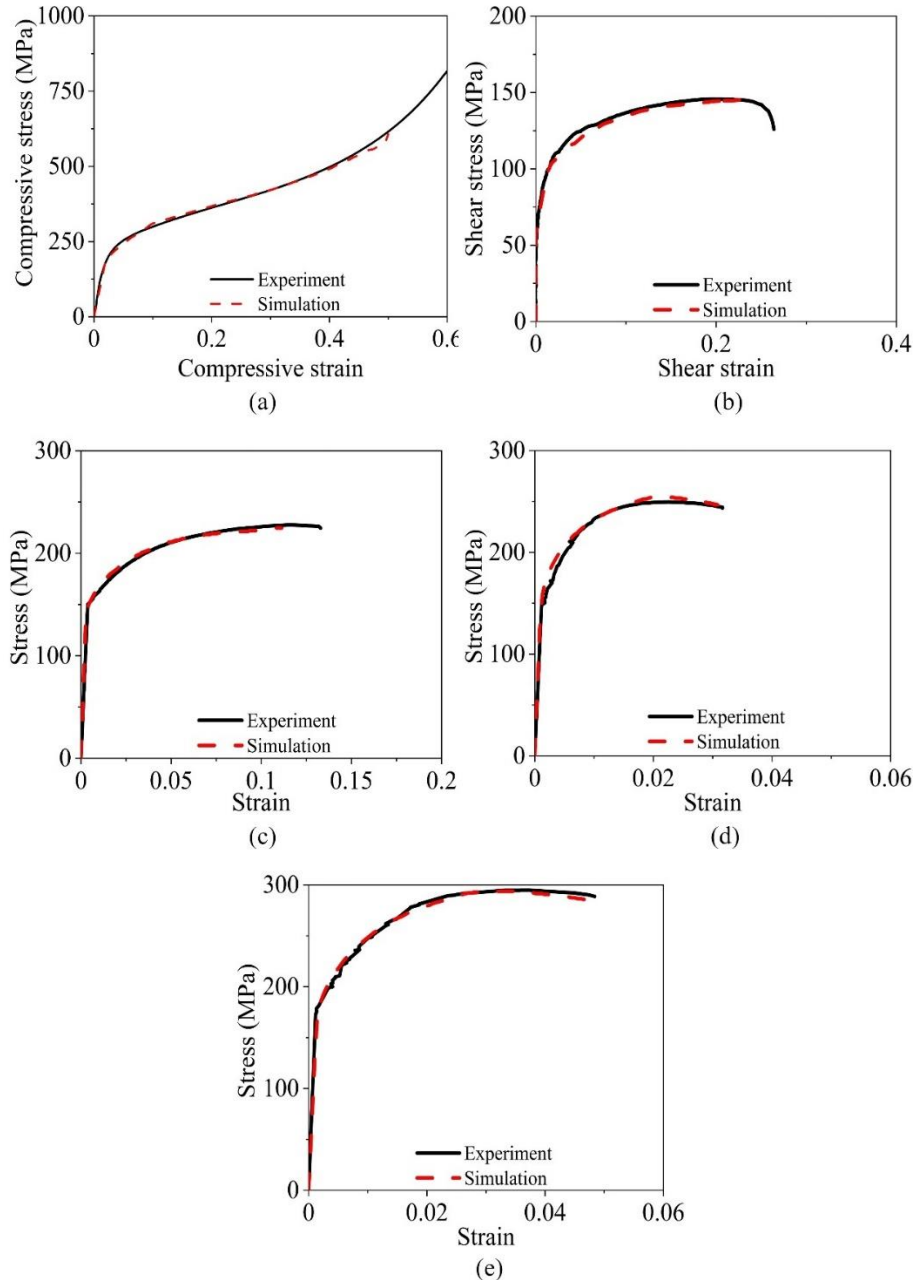


Figure 13. Numerical and experimental stress-strain curves: (a) uniaxial compression ($D/H=0.67$); (b) shear; (c) uniaxial tensile (non-notched); (d) uniaxial tensile (large notch); (e) uniaxial tensile (small notch).

Table 4. Details regarding experimental curves used for validation

| Type of FE model | Coupon details |
|-------------------------------|----------------------------------|
| Compression (D/H= 0.67) | Coupon 3 of inclined orientation |
| Shear | Coupon 1 of vertical orientation |
| Tensile - Non-notch | Coupon 2 of vertical orientation |
| Tensile – Notched (R = 12 mm) | Coupon 1 of vertical orientation |
| Tensile – Notched (R = 4 mm) | Coupon 3 of vertical orientation |

The validated models are subsequently used to calculate the triaxiality values. The locations used for triaxiality calculation is highlighted with a red dot in Fig. 3. Since no failure was observed during the compressive tests of D/H=1 coupons, therefore, numerical simulation for D/H=1 was not carried out. The stress contours obtained from the numerical simulations (at peak stress) and the calculated triaxiality values are shown in Fig. 14. The triaxiality values from zero strain till failure strain are averaged as the triaxiality for each loading condition and are -0.162 and 0.036 for uniaxial compression and shear, respectively. Tensile coupons without notch exhibit an average triaxiality of 0.329. Large notch and small notch coupons show average triaxiality values of 0.560 and 0.780, respectively.

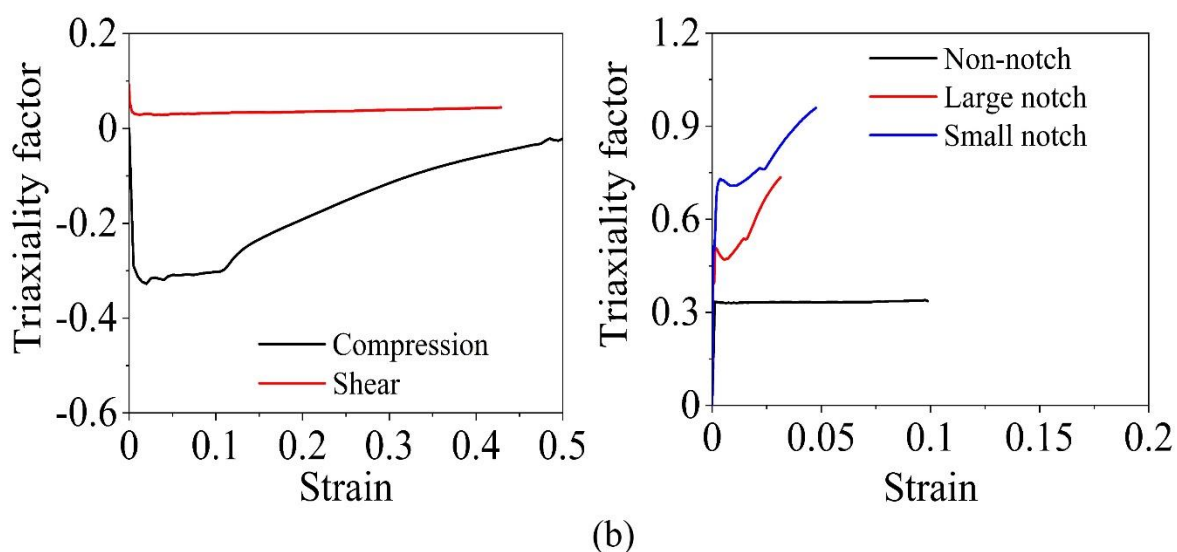
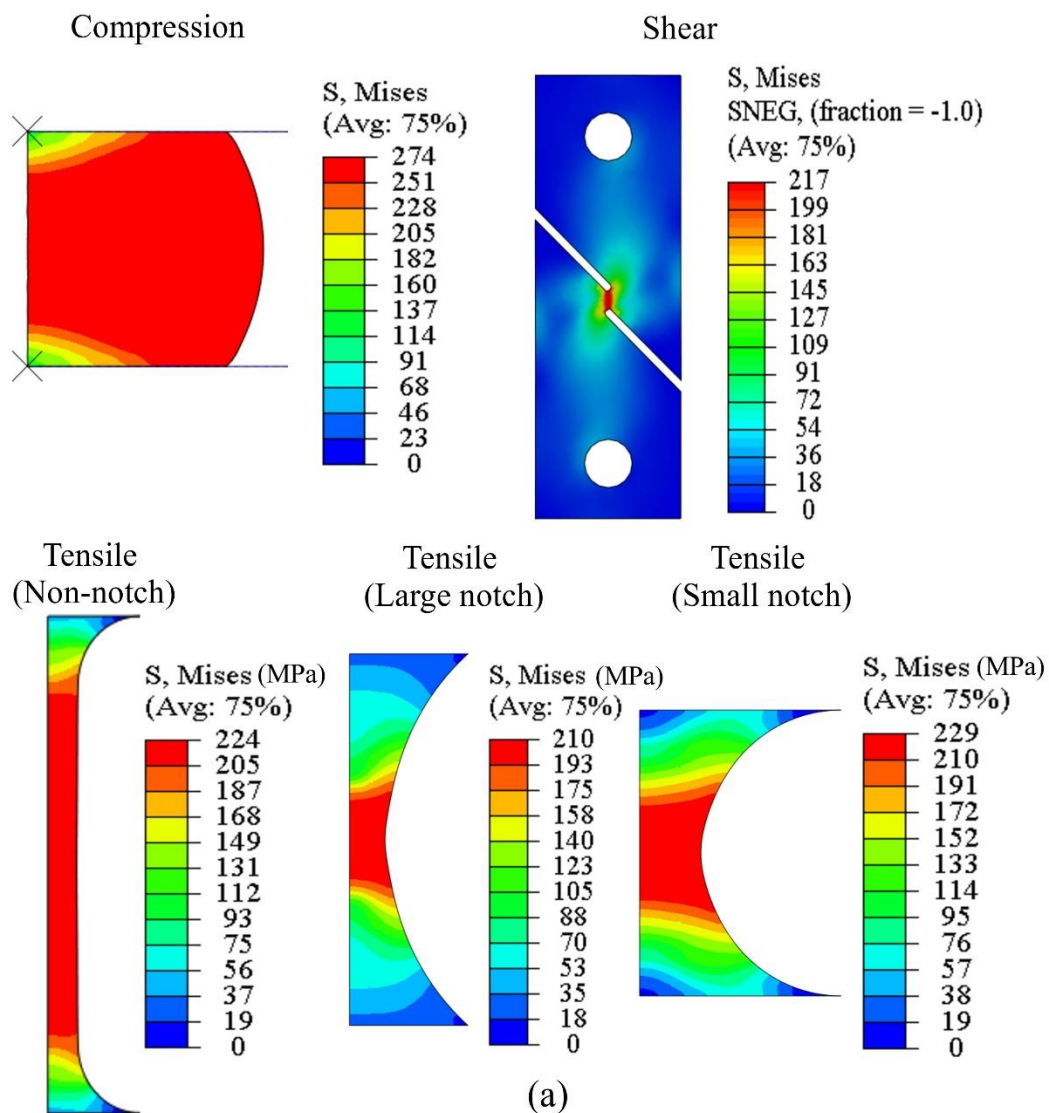


Figure 14. (a) Stress contour obtained from numerical simulations (Note: stresses are in MPa, and axisymmetric elements were used for tensile FE models and cut section shown for compression FE model); (b) triaxiality factors obtained from the numerical simulations.

4.4. Fracture loci

The fracture loci obtained for all the three build orientations are shown in Fig. 15. Polynomial curve fitting was used with failure strain and triaxiality factor as data points. It can be noticed that the trend of the loci is similar for all the build orientations. The maximum failure strain is observed at a negative triaxiality of -0.162 and the failure strain reduces monotonically as the triaxiality value increases. For the inclined and vertical orientations, the minimum failure strain is observed at a triaxiality of 0.570. However, for the horizontal orientation, the minimum failure strain was observed at a triaxiality of 0.790.

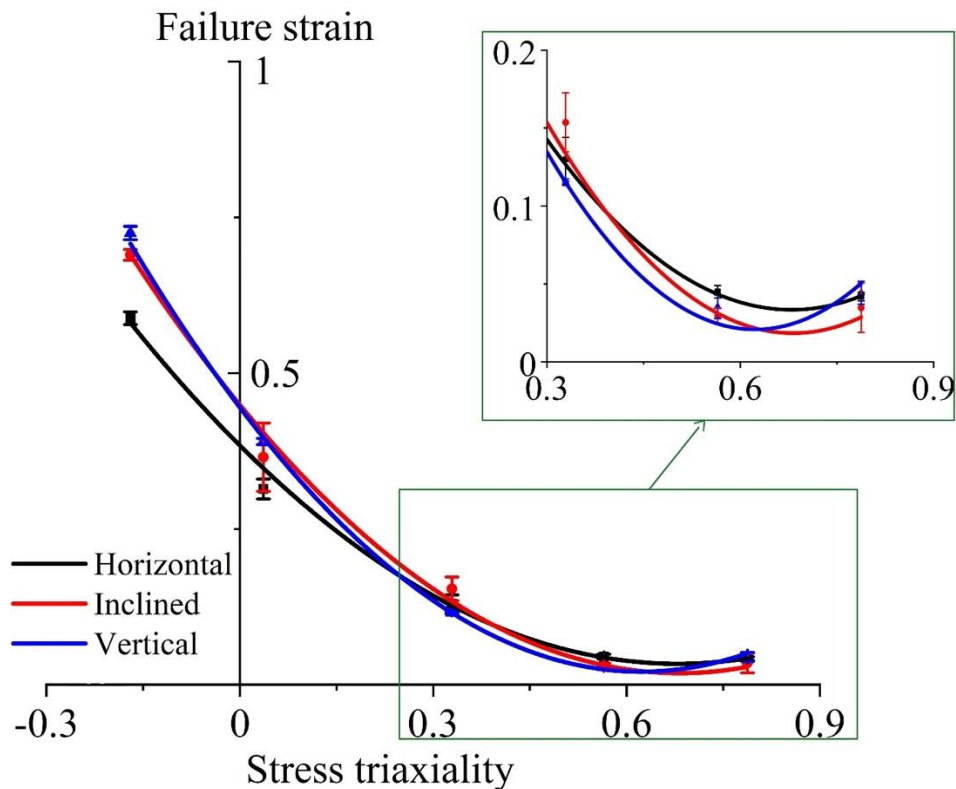


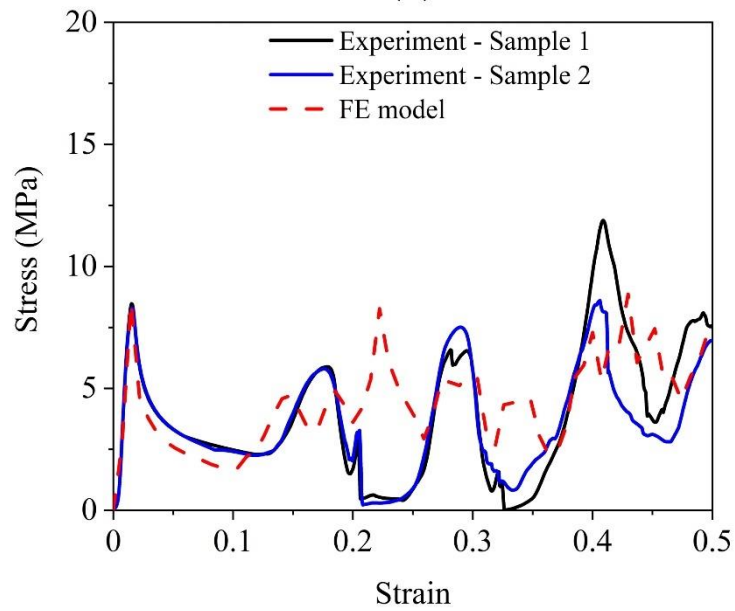
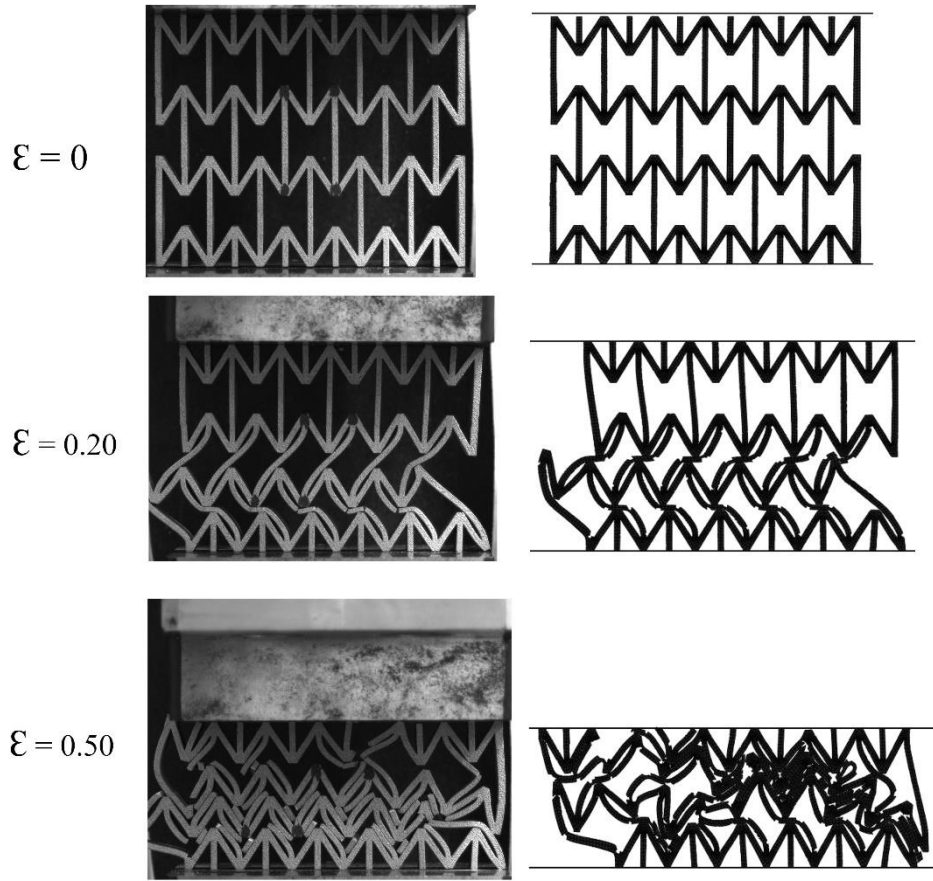
Figure 15. Fracture loci of additively manufactured Al10SiMg alloy for the three build orientations.

4.5. The application of fracture loci for the simulation of a re-entrant structure

Since most members in the re-entrant structure align with the vertical build orientation and fracture loci of coupons printed in the three build orientations do not show any major variation, fracture locus obtained for the vertical orientation was used for the FE analysis of

1 the re-entrant structure. Figure 16 shows the experimentally measured and numerically
2 simulated deformation mode and nominal stress-strain curves of the re-entrant structure. Two
3
4 tested samples show very similar deformation modes. Therefore, the deformation mode of
5
6 Sample 1 is presented in Fig. 16(a). In terms of deformation mode, both experiments and FE
7
8 results exhibit similar behavior. At the axial strain of $\varepsilon = 0.2$, vertical walls of the bottom two
9
10 rows buckle, and the top row remain intact. Failure of walls starts at the axial strain 0.2. The
11
12 optical image captured at the strain of 0.5 reveals that the structure failed at multiple locations.
13
14
15

16
17 Nominal stress-strain curve obtained from the FE analysis is compared with the
18
19 experimentally tested ones in Fig. 16(b). The initial peak stress of 8.5 MPa is noticed at an
20
21 axial strain of 0.015. After the initial peak, stress has dropped owing to buckling of vertical
22
23 walls. The FE predicted stress-strain curve of the structure is similar to the experimentally
24
25 measured one up to a strain of 0.2. Discrepancy in force values is observed at strains between
26
27 0.2 and 0.25, which is due to the slightly different deformation in simulation and experiment.
28
29 As it can be seen in Fig. 17, at an axial strain of 0.22, almost all vertical struts of the bottom
30
31 row fail (red oval) immediately in the experiments. However, in the FE model, some of the
32
33 vertical struts do not fail completely within this strain range (the red oval in Fig. 17b).
34
35
36
37
38
39
40
41
42
43
44
45
46
47
48
49
50
51
52
53
54
55
56
57
58
59
60
61
62
63
64
65



51
52
53
54
55
56
57
58
59
60
61
62
63
64
65

Figure 16. (a) Deformation modes (left images are experimental results and right images are simulated results); (b) nominal stress-strain curves of the re-entrant structure obtained from the experiments and numerical simulation.

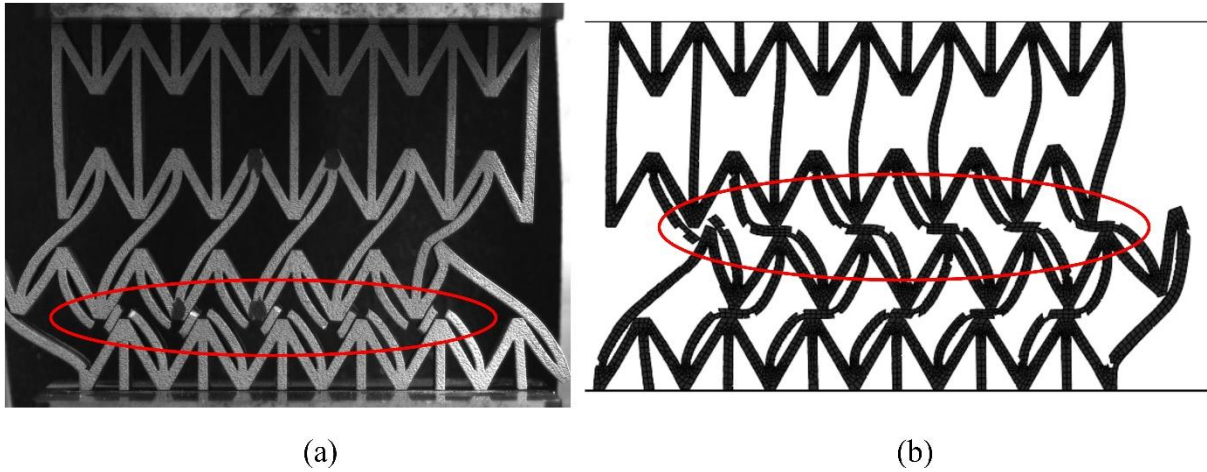


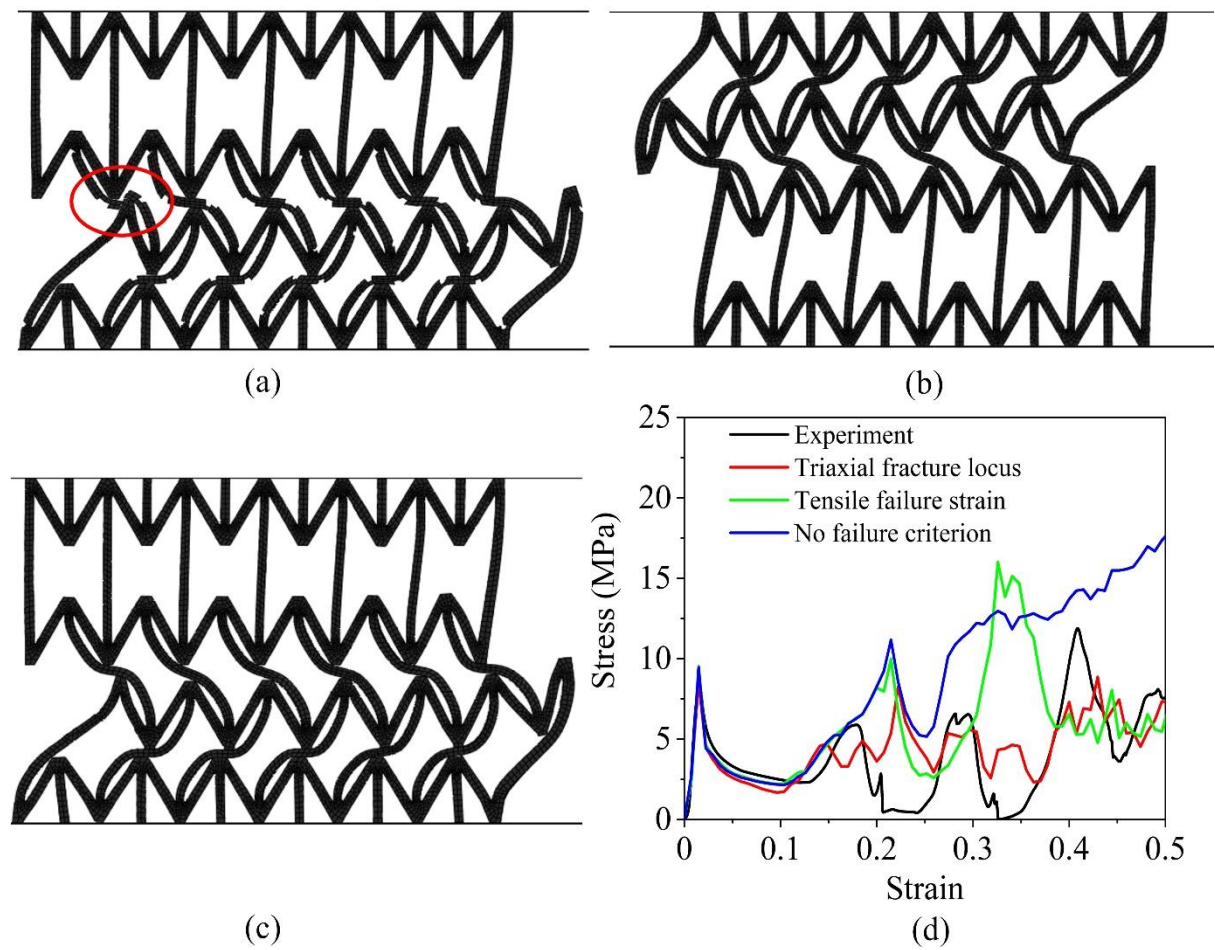
Figure 17. Deformation observed at the strain of 0.22: (a) experiment; and (b) simulation.

5. Discussion of the effect of failure strain on the simulation of a cellular structure

To evaluate the effect of the fracture locus, two more FE models of a cellular structure were further developed by using different failure criteria in the models, failure criterion in the first model utilized a failure strain obtained from the non-notch uniaxial tensile tests coupons (conventional tensile tests), and the failure criterion was not introduced in the second model (i.e., no failure criterion). The remaining settings of these two FE models such as material and geometrical parameters, loading and boundary conditions are the same as the FE models of the re-entrant structure mentioned in Section 3. The deformation at the axial strain of 0.2 obtained from the FE models with fracture locus and the uniaxial tensile failure strain are shown in Figs. 18(a) and (b). It can be seen that the vertical walls fail (red oval) when the triaxial locus is used, however, such failure is not observed in the FE model using uniaxial tensile failure criterion. The failed elements in the red oval (Fig. 18a) exhibit stress triaxiality of 0.55 and failure strain of 0.045. The FE model with tensile failure criterion has failed to predict this behavior (Fig. 18b). Also, it can be seen in Fig. 18(d), the FE models with tensile failure criterion and without failure criterion over-predict the strength. The results of FE models were compared with experiments in terms of plateau stress. Plateau stress in this work is defined as the average value of stress in the strain range of 0.015 to 0.6. The average plateau stress obtained through

1 experiments is 4.12 MPa. The plateau stress predicted by the FE model with the fracture locus
 2 is 5.32 MPa. The overprediction is due to the discrepancy in the stress-strain curve of the re-
 3 entrant structure between the axial strain of 0.2 and 0.25. On the other hand, the plateau stress
 4 predicted by the FE model with the tensile failure strain is 6.49 MPa, which is 57.5% more
 5 than experimental value and 22% more than the value predicted by the FE model with the
 6 fracture locus as the failure criterion. It is to be noted that the FE model without failure
 7 fracture locus as the failure criterion. It is to be noted that the FE model without failure
 8 predicted the plateau stress to be 11.97 MPa. This signifies the importance of the fracture locus
 9 to predict the deformation and strength of cellular structures.
 10
 11
 12
 13
 14
 15
 16
 17
 18
 19
 20
 21
 22
 23
 24
 25
 26
 27
 28
 29
 30
 31
 32
 33
 34
 35
 36
 37
 38
 39
 40
 41
 42
 43
 44
 45
 46
 47
 48
 49
 50
 51
 52
 53
 54
 55
 56
 57
 58
 59
 60
 61
 62
 63
 64
 65

The fracture locus of the material studied in this work exhibits very minor orientation
 dependency. However, for materials which exhibit significant orientation dependency, it is
 crucial to assign appropriate properties for walls built along particular orientations.



1
2
3
4
5
6
7
8
9
10
11
12
13
14
15
16
17
18
19
20
21
22
23
24
25
26
27
28
29
30
31
32
33
34
35
36
37
38
39
40
41
42
43
44
45
46
47
48
49
50
51
52
53
54
55
56
57
58
59
60
61
62
63
64
65

Figure 18. Deformation modes obtained from the FE models at the strain of 0.2: (a) with fracture locus and (b) with uniaxial tensile failure strain (0.17) as the failure criterion; (c) without any failure criterion; (d) nominal stress-strain curves obtained from the FE models with different failure criteria.

6. Conclusions

In this study, the mechanical behaviour of AlSi10Mg alloy processed via LPBF AM was characterized using a combined experimental and modelling framework. Both bulk and cellular structures were extensively tested and numerically analyzed. Initially, the effect of heat treatment of additively manufactured AlSi10Mg alloy was investigated to restore the ductility in the printed coupons. Test coupons were subjected to two different heat treatment processes namely, stress relieving (SR) and solution treatment (ST). Hardness and conventional tensile tests revealed that heat treated coupons were more ductile than as-printed coupons. Stress relieved coupons showed a good combination of strength and ductility. Therefore, all the test coupons and re-entrant structure employed in the study of fracture loci were stress relieved.

Fracture loci of additively manufactured AlSi10Mg were developed in this work. Series of tests including uniaxial compression tests of cylindrical coupons with two different D/H ratios, shear test, uniaxial tensile tests on non-notched and notched coupons were conducted. Numerical simulations of test coupons were also performed to determine the triaxiality values for all the test coupons. Failure strain versus triaxiality curves for all coupons printed along three orientations revealed that the dependency of fracture loci on the orientation was negligible.

A cellular re-entrant structure was tested under quasi-static compression and the results were used to validate the developed FE model with fracture locus. The FE models with and without tensile failure strain as damage criteria, were not able to precisely predict the deformation and failure observed in the experiments. This signifies the importance of triaxiality

1 based failure criterion to predict the failure of additively manufactured cellular structures.
2 Several other coupons (plate with hole, plane strain tension, equi-biaxial tension, equi-biaxial
3 compression, etc.) are being considered for future work to obtain detailed locus with respect to
4 stress triaxiality and lode angle.
5
6
7
8
9

10 11 **Acknowledgements**

12 The authors would also like to acknowledge and appreciate the financial support from
13 Ministry of Education (MoE), India through Scheme for Promotion of Academic and Research
14 Collaboration (SPARC/2018-2019/P988/SL).
15
16
17
18
19
20

21 **References**

- 22
23
24 [1] Logakannan KP, Ramachandran V, Rengaswamy J, Gao Z, Ruan D. Quasi-static and
25 dynamic compression behaviors of a novel auxetic structure. *Composite Structures*
26 2020;254:112853. <https://doi.org/10.1016/j.compstruct.2020.112853>.
27
28
29
30
31 [2] Yang L, Harrysson O, West H, Cormier D. Modeling of uniaxial compression in a 3D
32 periodic re-entrant lattice structure. *Journal of Materials Science* 2013;48:1413–22.
33 <https://doi.org/10.1007/s10853-012-6892-2>.
34
35
36
37 [3] Yang L, Harrysson O, West H, Cormier D. Compressive properties of Ti-6Al-4V auxetic
38 mesh structures made by electron beam melting. *Acta Materialia* 2012;60:3370–9.
39 <https://doi.org/10.1016/j.actamat.2012.03.015>.
40
41
42
43 [4] Liu W, Yang Z, Zhang J. The in-plane tensile and shear properties of novel chiral cellular
44 structures. *Mechanics of Advanced Materials and Structures* 2021;0:1–20.
45 <https://doi.org/10.1080/15376494.2021.1969607>.
46
47
48
49
50
51
52
53
54
55
56
57
58
59
60
61
62
63
64
65

- 1
2
3
4
5
6
7
8
9
10
11
12
13
14
15
16
17
18
19
20
21
22
23
24
25
26
27
28
29
30
31
32
33
34
35
36
37
38
39
40
41
42
43
44
45
46
47
48
49
50
51
52
53
54
55
56
57
58
59
60
61
62
63
64
65
- [5] Zhang J, Lu G, Ruan D, Wang Z. Tensile behavior of an auxetic structure: Analytical modeling and finite element analysis. *International Journal of Mechanical Sciences* 2018;136:143–54. <https://doi.org/10.1016/j.ijmecsci.2017.12.029>.
- [6] Zhang J, Lu G, Ruan D, Wang Z. Tensile behavior of an auxetic structure: Analytical modeling and finite element analysis. *International Journal of Mechanical Sciences* 2018;136:143–54. <https://doi.org/10.1016/j.ijmecsci.2017.12.029>.
- [7] Li X, Wang Q, Yang Z, Lu Z. Novel auxetic structures with enhanced mechanical properties. *Extreme Mech Lett* 2019;27:59–65. <https://doi.org/10.1016/j.eml.2019.01.002>.
- [8] Yang L, Harrysson O, West H, Cormier D. Mechanical properties of 3D re-entrant honeycomb auxetic structures realized via additive manufacturing. *International Journal of Solids and Structures* 2015;69–70:475–90. <https://doi.org/10.1016/j.ijsolstr.2015.05.005>.
- [9] Howell B, Prendergast P, Hansen L. Examination of acoustic behavior of negative poisson's ratio materials. *Applied Acoustics* 1994;43:141–8. [https://doi.org/10.1016/0003-682X\(94\)90057-4](https://doi.org/10.1016/0003-682X(94)90057-4).
- [10] Alderson KL, Pickles AP, Neale PJ, Evans KE. Auxetic polyethylene: The effect of a negative poisson's ratio on hardness. *Acta Metallurgica Et Materialia* 1994;42:2261–6. [https://doi.org/10.1016/0956-7151\(94\)90304-2](https://doi.org/10.1016/0956-7151(94)90304-2).
- [11] Logakannan KP, Ramachandran V, Rengaswamy J, Ruan D. Dynamic Performance of a 3D Re-entrant Structure. *Mechanics of Materials* 2020;148:103503. <https://doi.org/10.1016/j.mechmat.2020.103503>.

- 1
2
3
4
5
6
7
8
9
10
11
12
13
14
15
16
17
18
19
20
21
22
23
24
25
26
27
28
29
30
31
32
33
34
35
36
37
38
39
40
41
42
43
44
45
46
47
48
49
50
51
52
53
54
55
56
57
58
59
60
61
62
63
64
65
- [12] Liu YD, Yu JL, Zheng ZJ, Li JR. A numerical study on the rate sensitivity of cellular metals. *International Journal of Solids and Structures* 2009;46:3988–98. <https://doi.org/10.1016/j.ijsolstr.2009.07.024>.
- [13] Sun Y, Li QM. Dynamic compressive behaviour of cellular materials: A review of phenomenon, mechanism and modelling. *International Journal of Impact Engineering* 2018;112:74–115. <https://doi.org/10.1016/j.ijimpeng.2017.10.006>.
- [14] Tancogne-Dejean T, Li X, Diamantopoulou M, Roth CC, Mohr D. High Strain Rate Response of Additively-Manufactured Plate-Lattices: Experiments and Modeling. *Journal of Dynamic Behavior of Materials* 2019;5:361–75. <https://doi.org/10.1007/s40870-019-00219-6>.
- [15] Bai Y, Wierzbicki T. A comparative study of three groups of ductile fracture loci in the 3D space. *Engineering Fracture Mechanics* 2015;135:147–67. <https://doi.org/10.1016/j.engfracmech.2014.12.023>.
- [16] McClintock FA. A Criterion for Ductile Fracture by the Growth of Holes. *Journal of Applied Mechanics* 1968;35:363–71. <https://doi.org/10.1115/1.3601204>.
- [17] Rice JR, Tracey DM. On the ductile enlargement of voids in triaxial stress fields*. *Journal of the Mechanics and Physics of Solids* 1969;17:201–17. [https://doi.org/10.1016/0022-5096\(69\)90033-7](https://doi.org/10.1016/0022-5096(69)90033-7).
- [18] Johnson GR, Cook WH. Fracture characteristics of three metals subjected to various strains, strain rates, temperatures and pressures. *Engineering Fracture Mechanics* 1985;21:31–48. [https://doi.org/10.1016/0013-7944\(85\)90052-9](https://doi.org/10.1016/0013-7944(85)90052-9).

- 1
2
3
4
5
6
7
8
9
10
11
12
13
14
15
16
17
18
19
20
21
22
23
24
25
26
27
28
29
30
31
32
33
34
35
36
37
38
39
40
41
42
43
44
45
46
47
48
49
50
51
52
53
54
55
56
57
58
59
60
61
62
63
64
65
- [19] Bao Y, Wierzbicki T. On fracture locus in the equivalent strain and stress triaxiality space. *International Journal of Mechanical Sciences* 2004;46:81–98. <https://doi.org/10.1016/j.ijmecsci.2004.02.006>.
- [20] Bai Y, Wierzbicki T. A new model of metal plasticity and fracture with pressure and Lode dependence. *International Journal of Plasticity* 2008;24:1071–96. <https://doi.org/10.1016/j.ijplas.2007.09.004>.
- [21] Lou Y, Yoon JW, Huh H. Modeling of shear ductile fracture considering a changeable cut-off value for stress triaxiality. *International Journal of Plasticity* 2014;54:56–80. <https://doi.org/10.1016/j.ijplas.2013.08.006>.
- [22] Mohr D, Marcadet SJ. Micromechanically-motivated phenomenological Hosford-Coulomb model for predicting ductile fracture initiation at low stress triaxialities. *International Journal of Solids and Structures* 2015;67–68:40–55. <https://doi.org/10.1016/j.ijsolstr.2015.02.024>.
- [23] Wierzbicki T, Bao Y, Lee YW, Bai Y. Calibration and evaluation of seven fracture models. *International Journal of Mechanical Sciences* 2005;47:719–43. <https://doi.org/10.1016/j.ijmecsci.2005.03.003>.
- [24] Bao Y, Wierzbicki T. A comparative study on various ductile crack formation criteria. *Journal of Engineering Materials and Technology, Transactions of the ASME* 2004;126:314–24. <https://doi.org/10.1115/1.1755244>.
- [25] Wilson CD. A critical reexamination of classical metal plasticity. *Journal of Applied Mechanics, Transactions ASME* 2002;69:63–8. <https://doi.org/10.1115/1.1412239>.

- 1
2
3
4
5
6
7
8
9
10
11
12
13
14
15
16
17
18
19
20
21
22
23
24
25
26
27
28
29
30
31
32
33
34
35
36
37
38
39
40
41
42
43
44
45
46
47
48
49
50
51
52
53
54
55
56
57
58
59
60
61
62
63
64
65
- [26] Kiran R, Khandelwal K. A triaxiality and Lode parameter dependent ductile fracture criterion. *Engineering Fracture Mechanics* 2014;128:121–38. <https://doi.org/10.1016/j.engfracmech.2014.07.010>.
- [27] Butcher C, Abedini A. On Phenomenological Failure Loci of Metals under Constant Stress States of Combined Tension and Shear: Issues of Coaxiality and Non-Uniqueness. *Metals (Basel)* 2019;9:1052. <https://doi.org/10.3390/met9101052>.
- [28] Dunand M, Mohr D. On the predictive capabilities of the shear modified Gurson and the modified Mohr-Coulomb fracture models over a wide range of stress triaxialities and Lode angles. *Journal of the Mechanics and Physics of Solids* 2011;59:1374–94. <https://doi.org/10.1016/j.jmps.2011.04.006>.
- [29] Concli F, Gilioli A. Numerical and experimental assessment of the mechanical properties of 3D printed 18-Ni300 steel trabecular structures produced by Selective Laser Melting—a lean design approach. *Virtual and Physical Prototyping* 2019;14:267–76. <https://doi.org/10.1080/17452759.2019.1565596>.
- [30] Concli F, Gilioli A, Nalli F. Experimental–numerical assessment of ductile failure of Additive Manufacturing selective laser melting reticular structures made of Al A357. *Proceedings of the Institution of Mechanical Engineers, Part C: Journal of Mechanical Engineering Science* 2019;0:1–8. <https://doi.org/10.1177/0954406219832333>.
- [31] Roth CC, Tancogne-Dejean T, Mohr D. Plasticity and fracture of cast and SLM AlSi10Mg: High-throughput testing and modeling. *Additive Manufacturing* 2021;43. <https://doi.org/10.1016/j.addma.2021.101998>.
- [32] Dong Z, Liu Y, Li W, Liang J. Orientation dependency for microstructure, geometric accuracy and mechanical properties of selective laser melting AlSi10Mg lattices.

Journal of Alloys and Compounds 2019;791:490–500.

<https://doi.org/10.1016/j.jallcom.2019.03.344>.

[33] Maconachie T, Leary M, Zhang J, Medvedev A, Sarker A, Ruan D, et al. Effect of build orientation on the quasi-static and dynamic response of SLM AlSi10Mg. *Materials Science and Engineering A* 2020;788:139445. <https://doi.org/10.1016/j.msea.2020.139445>.

[34] Hartunian P, Eshraghi M. Effect of Build Orientation on the Microstructure and Mechanical Properties of Selective Laser-Melted Ti-6Al-4V Alloy. *Journal of Manufacturing and Materials Processing* 2018;2:69. <https://doi.org/10.3390/jmmp2040069>.

[35] Simonelli M, Tse YY, Tuck C. Effect of the build orientation on the mechanical properties and fracture modes of SLM Ti-6Al-4V. *Materials Science and Engineering A* 2014;616:1–11. <https://doi.org/10.1016/j.msea.2014.07.086>.

[36] Mfusi BJ, Tshabalala LC, Popoola API, Mathe NR. The effect of selective laser melting build orientation on the mechanical properties of AlSi10Mg parts. *IOP Conference Series: Materials Science and Engineering* 2018;430. <https://doi.org/10.1088/1757-899X/430/1/012028>.

[37] Shen LC, Yang XH, Ho JR, Tung PC, Lin CK. Effects of build direction on the mechanical properties of a martensitic stainless steel fabricated by selective laser melting. *Materials* 2020;13:1–18. <https://doi.org/10.3390/ma13225142>.

[38] Li Y, Pavier M, Coules H. Compressive fatigue characteristics of octet-truss lattices in different orientations. *Mechanics of Advanced Materials and Structures* 2021;0:1–13. <https://doi.org/10.1080/15376494.2021.1978020>.

- 1
2
3
4
5
6
7
8
9
10
11
12
13
14
15
16
17
18
19
20
21
22
23
24
25
26
27
28
29
30
31
32
33
34
35
36
37
38
39
40
41
42
43
44
45
46
47
48
49
50
51
52
53
54
55
56
57
58
59
60
61
62
63
64
65
- [39] Qi G, Ji B, Ma L. Mechanical response of pyramidal lattice truss core sandwich structures by additive manufacturing. *Mechanics of Advanced Materials and Structures* 2019;26:1298–306. <https://doi.org/10.1080/15376494.2018.1432805>.
- [40] Fousová M, Dvorský D, Michalcová A, Vojtěch D. Changes in the microstructure and mechanical properties of additively manufactured AlSi10Mg alloy after exposure to elevated temperatures. *Materials Characterization* 2018;137:119–26. <https://doi.org/10.1016/j.matchar.2018.01.028>.
- [41] Li W, Li S, Liu J, Zhang A, Zhou Y, Wei Q, et al. Effect of heat treatment on AlSi10Mg alloy fabricated by selective laser melting: Microstructure evolution, mechanical properties and fracture mechanism. *Materials Science and Engineering A* 2016;663:116–25. <https://doi.org/10.1016/j.msea.2016.03.088>.